

In vivo SS-OCT imaging of crystalline lens sutures

ASHISH GUPTA,¹  DANIEL RUMINSKI,¹  ALFONSO JIMENEZ VILLAR,¹  RAÚL DUARTE TOLEDO,² SILVESTRE MANZANERA,²  SPOZMAI PANEZAI,¹  JUAN MOMPEAN,² PABLO ARTAL,²  AND IRENEUSZ GRULKOWSKI^{1,*} 

¹*Institute of Physics, Faculty of Physics, Astronomy and Informatics, Nicolaus Copernicus University, ul. Grudziądzka 5, 87-100 Toruń, Poland*

²*Laboratorio de Óptica, Instituto Universitario de Investigación en Óptica y Nanofísica, Universidad de Murcia, Campus de Espinardo, E-30100, Murcia, Spain*

*igrulkowski@fizyka.umk.pl

Abstract: We demonstrate *in vivo* three-dimensional (3-D) visualization of crystalline lens sutures in healthy eyes using swept source optical coherence tomography (SS-OCT). Volumetric data sets of the crystalline lenses were acquired and processed to obtain enhanced contrast projection images and to extract suture patterns in both anterior and posterior lens. The results presented different types of the sutures including Y-sutures, simple and complex star sutures. Age-related changes in suture arrangement were characterized quantitatively. Crystalline lens suture imaging with SS-OCT might be a useful tool in fundamental studies on development and ageing of human lens.

© 2020 Optical Society of America under the terms of the [OSA Open Access Publishing Agreement](#)

1. Introduction

Human crystalline lens is responsible for around one third of the eye's refractive power. Functional properties of the crystalline lens are provided by two factors, i.e. tunability (variable focus) and transparency, which ensure optimum vision resulting in forming sharp image on the retina [1]. Alterations of these properties of the crystalline lens lead to the development of the most common age-related eye diseases such as presbyopia and cataract [2–4].

The crystalline lens is an active biconvex optical element able to change its shape during eye accommodation. The mechanism of accommodation is enabled by the apparatus made of ciliary muscles and zonular fibers. Aging processes in the eye make the lens more stiff and the ciliary muscles less contractile, which is thought to account for presbyopia, i.e. the loss of accommodation [5,6]. Moreover, the anatomy of the crystalline lens reveals that it is composed of epithelial cells in its anterior surface as well as fiber-like cells (Fig. 1(a)). The epithelial cells at the equatorial region divide and elongate in a form of fiber cells. Those secondary fibers meet at the planes in both anterior and posterior pole of the lens forming two inverted Y-shaped sutures, and they eventually comprise the fetal nucleus. As the lens grows throughout life, the number of fibers increases, and the suture pattern becomes more complex (star-shape sutures) [7–10].

Several biochemical and ultrastructure-based factors determine optical transparency of the crystalline lens [8]. Firstly, the fibers are highly and regularly packed inside the lens, which is enabled by the adhesive proteins in the fiber cell membrane [11]. Secondly, the processes of lens fibers' differentiation includes elimination of the nucleus and other intracellular light scattering structures (organelles). Thirdly, lens transparency can be explained by short-range interaction between crystallins and cytoskeletal proteins in the cytoplasm of the fibers that determines specific arrangement of crystallins and provides with tissue clarity [12]. Moreover, the lens is avascular tissue, which prevents light absorption by blood or lymph [13]. Lens physiology, especially microcirculation of water and ions, may play also a role in maintaining the lens transparency

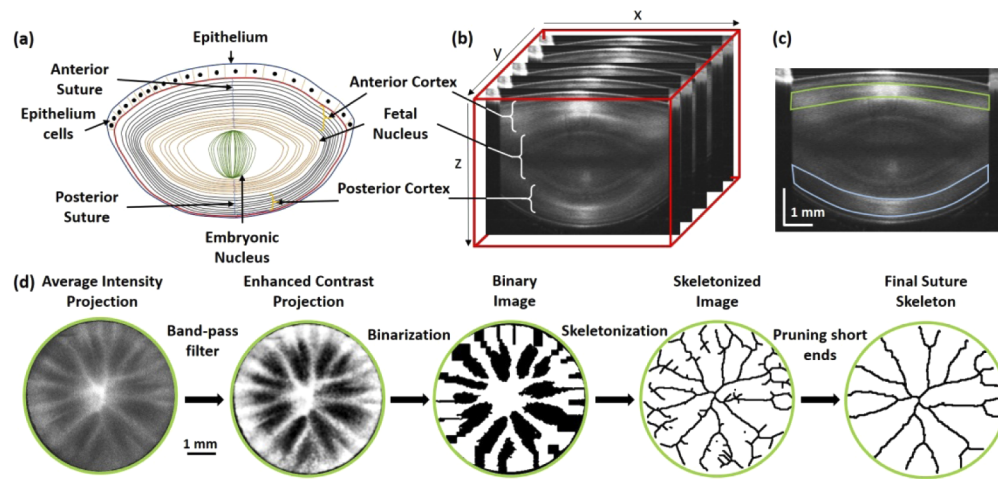


Fig. 1. (a) Anatomy structure of the human crystalline lens. (b) OCT volumetric data of the crystalline lens of $8 \times 8 \times 4 \text{ mm}^3$. (c) Segmented cortical layers of lens used to generate *en-face* projection images; green – anterior lens, blue – posterior lens. (d) Algorithm for image processing and extraction of suture pattern; averaged intensity *en-face* projection of anterior lens suture, image contrast enhancement with band pass filtering and CLAHE (contrast limited adaptive histogram equalization) contrast enhancement, image binarization, image skeletonization, pruning ends and false branches. Data presented here is anterior crystalline lens from the right eye of a 40-yo subject.

[6,14]. Ageing impacts the crystalline lens biochemistry, which results in the progressive loss of transparency of the lens due to disarrangement of the fibers and proteins inside the fiber cells. This condition manifests clinically as opacities, and leads to the development of age-related cataract, a major cause of vision impairment worldwide [15–19].

Suture pattern contributes to the optical quality of the crystalline lens [20–22]. In particular, previous studies suggest that sutures can induce optical aberrations [20,23–25]. The location of zones of discontinuity is correlated with the development of lens sutures [26]. Abnormal development of sutures has been shown to be associated with specific types of cataract [27]. In addition, surgical interventions like trabeculectomy and vitrectomy may result in post-surgical alterations in lens sutures that precede cataract formation [28,29].

Fundamental studies on the ultrastructure of the crystalline lens revealed its characteristic features, including sutures, with different imaging modalities. Lenticular suture visualization was performed using the techniques like point diffraction interferometry, light and electron microscopy [10,30–36]. Laser ray tracing was used to evaluate the effect of sutures on retinal image quality and aberration [20,37]. *In vivo* imaging of sutural cataract was performed using biomicroscopy [14,38,39]. Although those reports gave important insights about the relation between suture pattern of the lens and optical quality, the studies were mostly limited to *ex vivo* animal studies, *in vitro* specimens or only two-dimensional *en-face* imaging. Optical coherence tomography (OCT) can surpass those limitations and enable a high-resolution three-dimensional (3-D) *in vivo* imaging of lens suture architecture in a non-contact and non-invasive way [40].

The aim of this study is to demonstrate *in vivo* imaging of the human crystalline lens sutures from the 3-D OCT data and to describe sutural structure quantitatively. Age-related changes in suture architecture in the anterior and posterior lens are characterized.

2. Methods

2.1. Study group

A total number of 100 eyes of 50 participants was enrolled in this study (mean age: 40 years, age range: 9-78 years). The participants underwent standard ophthalmic examination. Volunteers with previous ocular surgery were excluded from the study. The characteristics of the group recruited for the study is given in Table 1.

Table 1. Demographic data of the study group.

Parameter	Mean \pm SD ^a
Number of participants	50
Number of eyes	100
Age (yo)	40.0 \pm 19.3
Sphere (D)	-1.02 \pm 2.14
Cylinder (D)	-0.60 \pm 0.55

^aSD – standard deviation

This cross-sectional observational study was conducted at the University of Murcia and adhered to the tenets of the Declaration of Helsinki. The study was approved by the Institutional Review Boards at the Nicolaus Copernicus University and at the University of Murcia. The volunteers were informed about the nature of the study, and a written consent was obtained from each participant.

2.2. OCT imaging

All imaging procedures were performed by a single experienced operator. The OCT imaging was performed with the SS-OCT instrument enabling whole anterior segment visualization [41,42]. The system operated at the central wavelength of 1050 nm and at the sweep rate of 50 kHz. The imaging depth range of the system was 22.2 mm in air. The obtained sensitivity was 103 dB. The axial and transverse resolutions were 8 μ m and 43 μ m, respectively. The power incident on the cornea (1.9 mW) did not exceed ANSI standards. The preview mode in real time was enabled by the FPGA module of the acquisition card. The alignment of the subject eye was also facilitated by the iris camera integrated in the OCT system interface. No pupil dilation was used in this study. The scanning procedures were completed under constant conditions of dim illumination. The eyes were imaged in the relaxed accommodation state, which was controlled by an additional channel in the interface of our SS-OCT scanner.

2.3. Data post-processing and suture pattern extraction

Each 3-D volumetric OCT data set consisted of 300 \times 300 A-scans and covered 8 \times 8 mm² area (Fig. 1(b)). Therefore, the acquisition of a single volumetric data set took 1.8 seconds. In the post-processing, 3-D data sets were corrected for motion artifacts. In detail, two central cross-sectional images taken along slow- and fast-scan directions were extracted from the volume and blurred with Gaussian window. The anterior interface of the lens was segmented in those images using Sobel filter, and the ellipsoid surface was fitted. The difference between the fit and segmented anterior lens interface was used to correct B-scans for axial motion of the eye. Later on, *en-face* projection image was generated from volumetric data and binarized to determine the transverse motion artifacts. Therefore, for each B-scan, the edges of the pupil mask could be easily obtained from binarized *en-face* image, and enabled to find a proper shift with respect to the center of the volume. The procedure of motion artifact correction allowed to obtain a circular shape of the pupil.

Both anterior and posterior intensity projection images were generated from axially averaged slabs (ca. 320 μm thick) below the anterior interface and above the posterior interface of the lens, respectively (Fig. 1(c)). Therefore, the entire depth of the cortex was not included in the slabs. The exact position and thickness of the slab within the lens cortex layer used for OCT average intensity projection (AIP) was set individually to obtain the optimum AIP image contrast by visual inspection. Similar manual approach was applied to lens nucleus for generation of Y-shaped sutures (the slabs were ca. 80 μm thick in this case; not shown in Fig. 1).

A semi-automatic image processing algorithm was developed in ImageJ to get suture pattern from selected (anterior or posterior) cortical layer of the crystalline lens (Fig. 1(d)). First, band-pass filter was applied to enhance contrast between suture branches and background signal in the AIP image. Band-pass filter was set to have large structures filtered down and small structures filtered up to 40 pixels and 3 pixels, respectively. Direction tolerance of the filter was set to 5%. Image intensity was rescaled after filtering to match the range of display values. Further enhancement of images was done with contrast limited adaptive histogram equalization (CLAHE) algorithm (no mask, block size 127, histogram bins 256, normal speed for high accuracy) [43]. Then, enhanced AIP image was binarized by thresholding the signal. Robust automatic threshold selection (RATS) algorithm was applied to set the threshold level (estimate of the noise 5, scaling factor 3, and min leaf size 60) [44]. Later on, binary projection underwent automatic skeletonization based on thinning algorithm, which enabled obtaining suture pattern with false short ends or small branches [45]. Therefore, a final step to obtain suture pattern included pruning of those false short ends / branches using 'shortest branch' prune cycle method. Some remaining false short branches were also removed manually. The procedure described above was applied to both anterior and posterior projection images so that we obtained two suture skeletonized images (anterior and posterior) from each eye.

Validation of the proposed algorithm was performed by the assessment of the ability of the algorithm to detect the sutures. The suture branches were counted using the obtained skeleton patterns and compared with the number of sutures detected manually by a trained grader in corresponding AIP images. The grader did not know the age or the output of the algorithm. Agreement between both methods of suture segmentation was assessed using Bland-Altman analysis.

Different parameters were extracted to describe the architecture of the crystalline lens sutures quantitatively:

a) anterior cortex mean signal

The AIP image from anterior lens was masked by the inverse mask of the anterior sutures. The average signal was calculated. This quantity shows the average signal in anterior AIP image in the regions outside sutures.

b) anterior suture mean signal

The AIP image from anterior lens was masked by the suture pattern mask. The average signal was calculated. This quantity shows the average signal from sutures in AIP image.

c) posterior cortex mean signal

The AIP image from posterior lens was masked by the inverse mask of the posterior sutures. The average signal was calculated. This quantity shows the average signal in posterior AIP image in the regions outside sutures.

d) posterior suture mean signal

The AIP image from posterior lens was masked by the suture pattern mask. The average signal was calculated. This quantity shows the average signal from sutures in AIP image.

e) suture density index

The number of pixels indicating sutures in skeletonized image were divided by the number of pixels covering the pupil area.

The above-mentioned parameters were calculated in the circular region of interest of the diameter of 3.5 mm, which corresponded to the smallest pupil in the group.

We entered all data into a Microsoft Excel 2019 spreadsheet (Microsoft Corp., Redmond, WA). Pearson's correlation coefficient R between extracted parameters and the subject age was calculated and statistical significance of R was assessed (p -value). Statistical significance was taken to be a level of $\alpha = 0.05$.

3. Results

We imaged one hundred eyes in this study. We successfully extracted the information on the suture pattern from 91 volumetric images (91% of all data sets). The data in 9 eyes had to be rejected due to poor image quality and low signal.

3.1. Suture visualization

The representative image (central cross-section) of the crystalline lens is shown in Fig. 2.

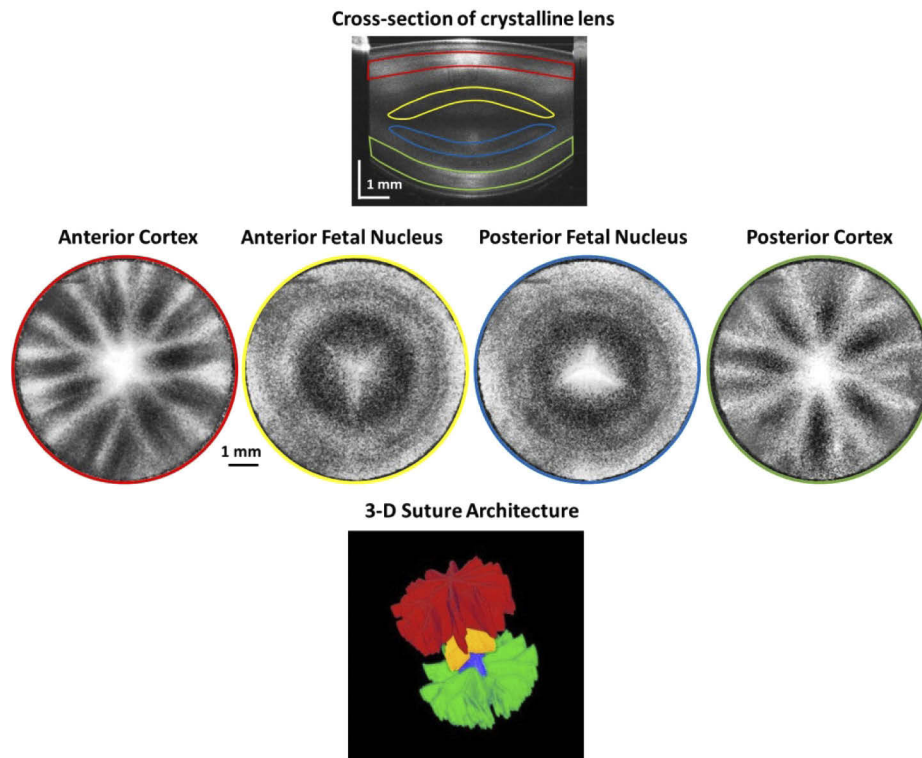


Fig. 2. Cross-sectional OCT image of the human crystalline lens of the right eye of a 40-yo subject. The slabs used to generate the AIP images are indicated in color (upper row). Corresponding *en-face* projection images of anterior cortex (red), anterior fetal nucleus (yellow), posterior fetal nucleus (blue), and posterior cortex (green). Characteristic Y-suture pattern visible in the fetal nucleus. 3-D rendering of this data set is shown also in [Visualization 1](#).

The projection images from anterior and posterior cortex demonstrate complex patterns of star sutures in the anterior and posterior lens. The sutures are hyper-intensive lines that radiate from the pole toward the equator (Fig. 2, middle row). Additionally, we generated similar projections from the 80 μm -thick slabs corresponding to the fetal nucleus of the lens where the sutures are initially formed. In this case, we were able to identify also Y-shaped sutures (and inverted Y-sutures) that are characteristic for early development of the lens (Fig. 2, middle row). Y-sutures were visible in 56 volumetric images (61% of all data sets). Visualization 1 and Fig. 2 (bottom row) illustrate volumetric rendering of the crystalline lens with overlaid 3-D suture architecture. The sutures form the planes that in projection appear as branches.

The sutures from anterior and posterior hemisphere of the lens can be superimposed (Fig. 3(a)). In the case presented in Fig. 3(a), we also observe that the suture pattern from the posterior lens is rotated ca. 20 degrees clockwise with respect to the suture pattern from the anterior lens. Moreover, it is possible to represent the suture complex organization in polar coordinate system (Fig. 3(b)). Dendritic pattern of sutures as well as correspondence between anterior and posterior suture branches can be explored with this transformation. However, one has to remember that OCT does not enable exploration of sutures up to the lens equator since lens sampling area is limited by the pupil size and no peripheral regions are imaged. Additionally, no refraction correction was applied to the data. As a consequence, the polar representation does not cover the entire lens interfaces, and the information on how the anterior and posterior sutures are connected cannot be retrieved.

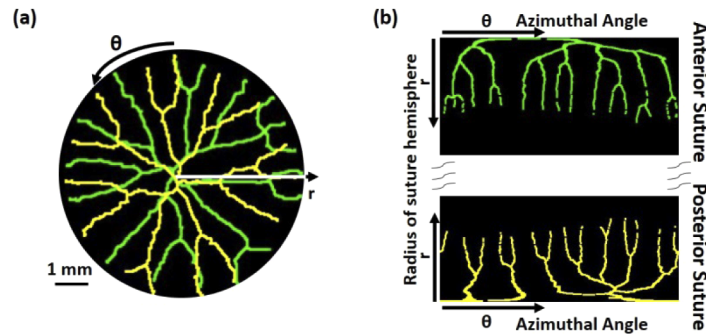


Fig. 3. Anterior (green) and posterior (yellow) suture pattern in the crystalline lens of the right eye of a 40-yo subject. (a) Representation in Cartesian coordinate system. (b) Representation in polar coordinate system. Posterior suture pattern was not corrected for light refraction.

The examples of images and corresponding anterior suture patterns of human lenses of different ages are presented in Fig. 4. The structural changes in the crystalline lens throughout the life are based on adding consecutive layers of fiber cells (shells). This growth is visualized in the overview of cross-sectional images in Fig. 4 (upper row) where the lens thickness increases. Another factor associated with the lens ageing is its transparency. Visual inspection and comparison of OCT B-scans and projection images demonstrate progressively stronger lens signal with age so that intraocular scattering increases. In particular, the cortex and the nucleus become more reflective, which can be easily noticed by comparing the images of young and old subjects (Fig. 4, middle row).

The analysis of the suture patterns indicates age-dependent development of sutures in the crystalline lens. The lens of a 10-yo person in Fig. 4 features simple six (or seven-) branch suture pattern, which is the simplest form of star sutures [10]. The suture architecture becomes even more complex in the adolescence. The number of branches of the complex star pattern increases reaching 9, 12 or sometimes even more branches.

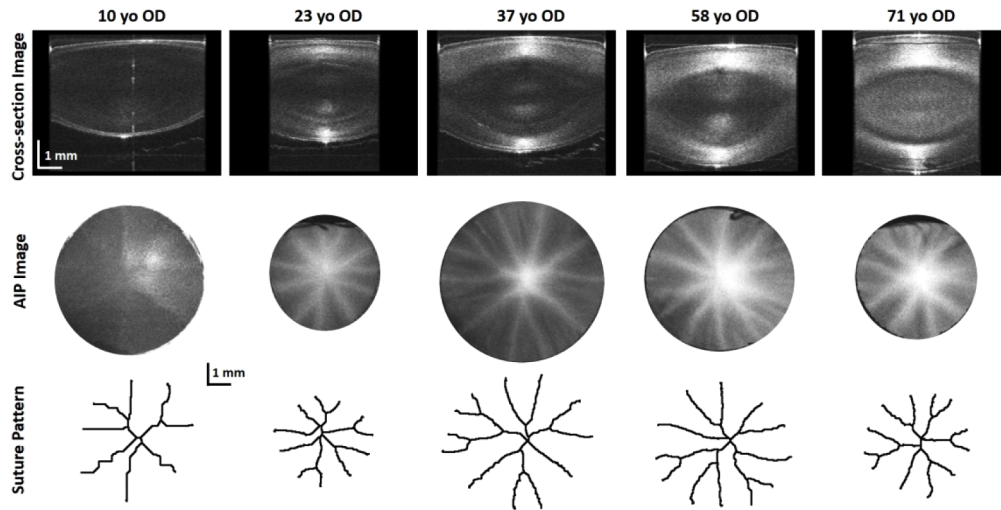


Fig. 4. Crystalline lens and suture pattern in the ageing eye. OCT cross-sectional image (upper row), AIP images (middle row) and extracted anterior suture patterns (bottom row) of human lenses in different decades of human life.

Detailed examination of obtained projections made it also possible to notice hypo-reflective zones surrounded by regular hyper-reflective lines within the sutures (red arrow in Fig. 5 and Visualization 2). This effect was observed in 22 eyes (24% of all data sets used for analysis).

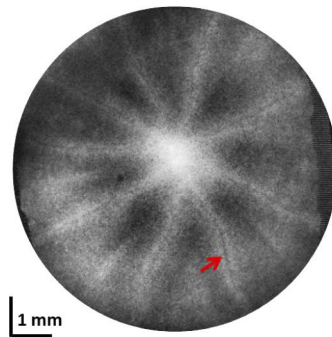


Fig. 5. Enhanced-contrast AIP of the right eye of 28-yo subject. Projection fly through the depth is shown in Visualization 2.

3.2. Validation of algorithm for suture pattern extraction

We performed validation of the developed algorithm for extraction of sutures from AIP images. The validation procedure was based on counting the number of detected suture branches (in skeleton patterns) in both anterior and posterior pole of the lens. Additionally, manual detection of sutures was performed using generated AIP images. Figure 6 demonstrates correlation between applied approaches (left column) as well as the Bland-Altman plots (right column). High and statistically significant correlation was found. The semiautomatic algorithm demonstrates also a very good agreement with manual grading of the suture pattern. The maximum difference between both methods does not exceed 2.

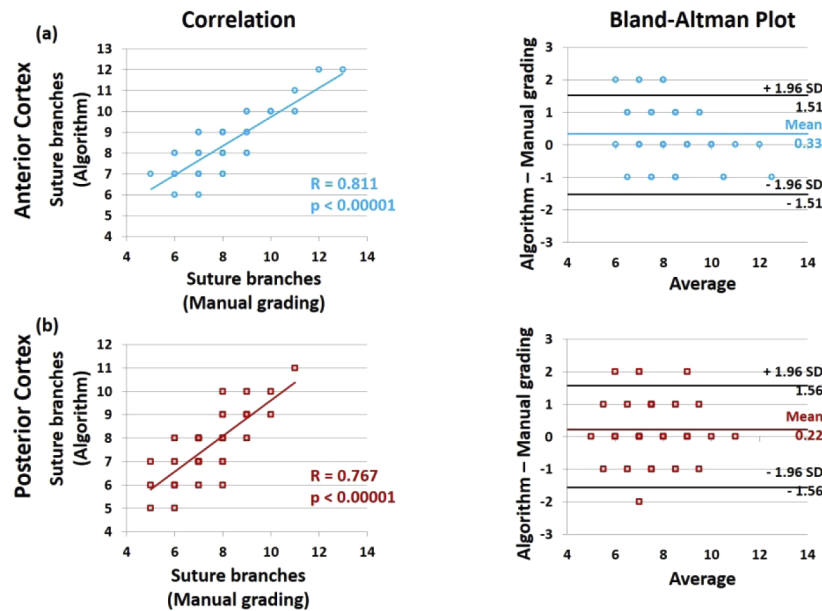


Fig. 6. Validation of the algorithm for suture pattern extraction. Comparison and agreement between semi-automatic algorithm and manual grading of the AIP images: (a) anterior lens sutures and (b) posterior lens sutures. The plots demonstrate correlation between detected number of suture branches (left column) and Bland-Altman plots (right column).

3.3. Quantitative analysis of crystalline lens sutures

We calculated the number of branches in the anterior and posterior lens. Statistically significant correlation between the number of observed primary branches in both parts of the crystalline lens was found (Fig. 7(a)). Additionally, less sutures were identified in the posterior lens with respect to the number of visualized sutures in the anterior lens. The number of detected branches increases slightly with age but the correlation is not statistically significant (Fig. 7(b)).

We also introduced the parameter called suture density index, which describes the total length of sutures related to the number of pixels covering the circular region of interest. The results present statistically significant (but weak) correlation of suture density index with age for anterior suture patterns. However, no correlation with the age is observed in the posterior part of the crystalline lens (Fig. 7(c)).

Furthermore, we performed the analysis of the signal in AIP images in the anterior and posterior cortex (Fig. 7(d-e), respectively). The plots show that the averaged signal from the cortex as well as the averaged signal taken along the corresponding sutures are highly correlated with age. In addition to that, the increase rate of the suture signal is higher than that of cortex signal.

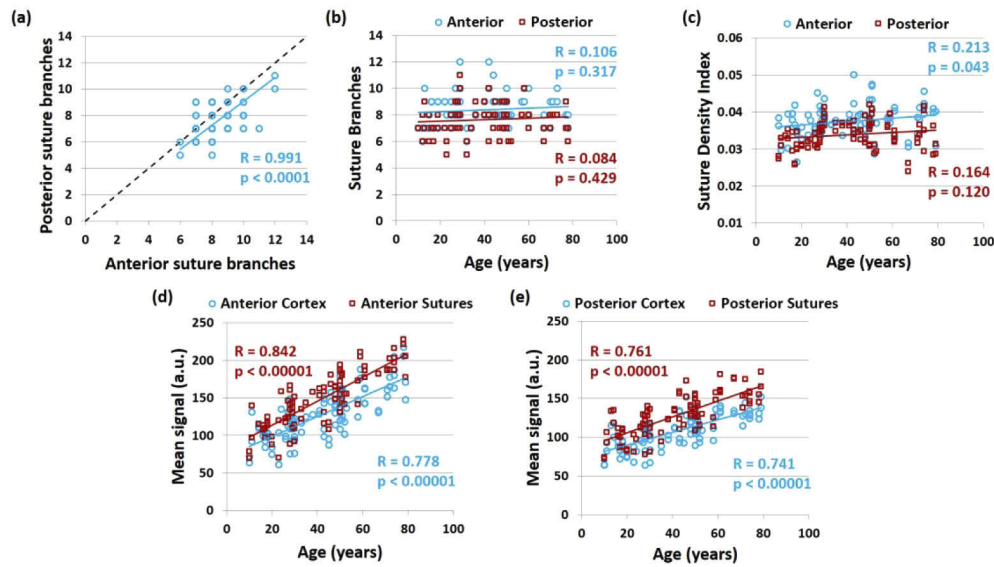


Fig. 7. Quantitative analysis of suture pattern of human lens *in vivo*. (a) Relation between the number of branches in the posterior lens and the number of branches in the anterior lens. Dashed line represents equality of the numbers. (b) Age-related changes in the number of branches. (c) Age-related changes of the suture density index. (d) Age-related changes in the mean signal of the anterior cortex and of the anterior suture pattern derived from AIP images. (e) Age-related changes in the mean signal of the posterior cortex and of the posterior suture pattern derived from AIP images.

4. Discussion and conclusions

In this paper, we demonstrated 3-D visualization of sutures in the human crystalline lenses *in vivo* using OCT. A comprehensive *in vivo* analysis on human lens suture organization in ageing eye has not been reported before although anterior segment SS-OCT was widely used for crystalline lens imaging [41,42,46–51]. The ability of OCT to image the sutures was shown before in rodent and human eyes [40–42]. Previous reports on human lenticular sutures were mostly limited either to *ex vivo* or to *in vitro* conditions. Moreover, microscopic modalities used in earlier studies did not enable volumetric imaging and large field of view although they provided with extremely high resolution images [7,8,20,31,33,52,53].

SS-OCT features several advantages that address the challenges of suture visualization and facilitate that new imaging application even in subjects with no diagnosed cataract. Firstly, the principle of operation based on detection of back-scattered photons makes OCT perfectly suited for suture imaging. In fact, lenticular sutures appear in projection images as regions with higher reflectivity. Elevated light scattering in the suture branches, which we observe in OCT projection images, is consistent with the fact that lenticular sutures are formed by the abutting ends of cell fibers, which was confirmed in several microscopic studies [30]. This ultrastructural natural discontinuity can be directly related to optical heterogeneity, which results in higher scattering as light passes through these regions. Hence, the obtained results (images) are consistent with cellular (ultrastructural) details of fiber arrangement in the crystalline lens and its impact on optical quality of the lens.

Secondly, SS-OCT is a modality characterized by higher sensitivity than other OCT generations so that it is possible to efficiently image semi-transparent objects like crystalline lenses in their natural state. Lens sutures are practically invisible in healthy conditions using regular lens

imaging with a slit lamp, however, clinical cases with sutural cataract can demonstrate opaque sutures clearly distinguishable in biomicroscopic examination [14]. Therefore, OCT extends this ability into the less scattering cases, which in turn enhances diagnostic utility. With the high scan density, 3-D OCT data enable also implementation of different strategies to selected subsets of voxels that can contrast desired structures effectively. In this study, we used voxel axial averaging to increase signal-to-noise ratio that resulted in a higher projection image quality with no significant loss of resolution.

Thirdly, SS-OCT at the wavelength of 1 μm represents a trade-off between light penetration (scattering, water absorption) and image resolution. Light scattering decreases with the illuminating wavelength, which allows for larger penetration depths at longer wavelengths and enables less attenuation by ocular opacification. However, tissue imaging at 1 μm or 1.3 μm is limited by water absorption, and axial resolution is poorer compared with 0.84 μm bandwidth.

Fourthly, the sutures are actually three-dimensional anatomical structures, thus requiring volumetric imaging for visualization. Accordingly, SS-OCT with its low sensitivity drop with depth shows the potential for effective reconstruction of the sutures' architecture. Finally, OCT can probe optical properties in a non-contact and non-invasive way. As a consequence, unlike with other optical methods, the studies on lens sutures can be done *in vivo*.

Clinical research on ageing lens involving imaging modalities included the topics such as lens biometric alterations, increased scattering or loss of accommodation [2,19,22,50]. We studied another aspect of the processes of eye ageing that takes into account formation of sutures. We showed the types of sutures that appear at different stages of human lens development and ageing: Y-shaped sutures in fetal nucleus, simple and complex star-shaped sutures as the effect of continuous division and differentiation of epithelium cells. Formation of more complex suture patterns in the crystalline lenses complies with the age-dependent structural organization of sutures, as revealed by earlier ultrastructural studies [10,53]. The discrepancy between the number of sutures detected in the anterior and posterior lens cortex could be partially attributed by the lower signal in OCT images in the posterior part of the crystalline lenses. When the numbers of sutures in the anterior and posterior part of the crystalline lens matched, it was possible to find offset (rotation angle) between patterns [32]. Moreover, the results in Fig. 4 confirmed well-known changes in lens morphology (e.g. thickness) and transparency with ageing [2]. We have to point out that a single cross-section of the crystalline lens does not allow to reveal the architecture of sutures. This is a volumetric image that enables to generate virtually any projection, thus providing insight into sutures.

It has been shown experimentally that sutures play role in lens aberrations [25]. However, recent findings demonstrated possible involvement of the sutures in circulation of nutrients and removal of waste, which is crucial for lens physiology [14,54,55]. This hypothesis might be confirmed by the observation of hypo-reflective zones surrounded by regular hyper-reflective lines, which remind extracellular zones of discontinuity. This unexpected optical effect could be associated with light absorption, light polarization, small gap within fiber cells interconnection along the suture or with flow (microcirculation). Consequently, more detailed investigation is required for that effect.

The main limitation of the current study was a limited field of view. OCT was not able to image through the iris so that the eye pupil constitute the effective imaging area, and the lens periphery cannot be inspected. It is important to mention here that we have not used any mydriasis in this study, and it is well known that natural pupil size decreases with age [56]. Pupillary dilation seems to be the optical condition for this type of study as it would relax accommodation and maximize the pupil size while making it insensitive to light conditions. However, in the study protocol we wanted to avoid reducing the comfort of healthy individuals recruited for the study. Furthermore, the developed algorithm included the steps of skeletonization and pruning, which were the sources of some erroneous detection of sutures (cf. Fig. 4), although the number of

detected sutures correlated very well with manual detection. The shape of some sutures did not fully correspond to that observed in the periphery of AIP image especially in the eyes of young subjects where the OCT signal of the crystalline lens was relatively low. Suture branches were more clearly visible in older subjects due to higher scatter and better AIP image contrast.

The pupil diameter introduced a bias in the quantitative analysis of the crystalline lens sutures with respect to the age. Therefore, the same diameter of the region of interest was used in this study to calculate the biomarkers. The results showed that suture density index correlates very weakly with the age only for anterior sutures and confirms the fact that we did not observe significantly higher numbers of suture branches in older subjects. The effect of age on suture development might be more pronounced if more younger participants are included. The age-related changes in the cortical and sutural OCT signal confirm opacification processes in the crystalline lenses, which reduce their transparency [41,42].

It is important to mention that the volumetric data were not corrected for light refraction. The OCT images shown in this study represent optical distances. Consequently, the effective imaging range of the posterior lens is lower than that of the anterior lens. Based on ray tracing applied to the model eye, one can estimate that the observed transverse range of the posterior lens is ca. 12% smaller than the pupil diameter (in the anterior lens). Since the circular pupil is the physical barrier to the evaluation of the crystalline lens, the imaged area in the posterior surface of the lens is ca. 22% smaller than the pupil area. Moreover, the biomarkers introduced in this study to describe the sutures are not based on geometrical dimensions, which are affected by light refraction in the lens.

In conclusion, SS-OCT is a powerful imaging technique for comprehensive 3-D visualization of the architecture of crystalline lens sutures. This technology for lens imaging is a useful tool for performing *in vivo* fundamental studies on development and ageing of human lens as well as clinical studies on the formation of cataracts.

Funding

Fundacja na rzecz Nauki Polskiej (POIR.04.04.00-00-5C9B/17-00); Narodowe Centrum Nauki (2015/18/E/NZ5/00697); Secretaría de Estado de Investigación, Desarrollo e Innovación (FIS2016-76163-R); Fundación Séneca (19897/GERM/15); European Regional Development Fund (EU-FEDER); European Social Fund-PROM (POWR.03.03.00-00-PN/13/18).

Disclosures

The authors declare that there are no conflicts of interest related to this article.

References

1. P. Artal, "Optics of the eye and its impact in vision: a tutorial," *Adv. Opt. Photonics* **6**(3), 340–367 (2014).
2. C. A. P. Cavallotti and L. Cerulli, eds., *Age-Related Changes of the Human Eye* (Humana Press, 2008).
3. L. A. Levin, S. F. E. Nilsson, J. Ver Hoeve, S. M. Wu, A. Alm, and P. L. Kaufman, eds., *Adler's Physiology of the Eye* (Elsevier, Edinburgh, 2011).
4. J. F. Hejtmancik, S. A. Riazuddin, R. McGreal, W. Liu, A. Cvekl, and A. Shiels, "Lens Biology and Biochemistry," in *Progress in Molecular Biology and Translational Science*, J. F. Hejtmancik and J. M. Nickerson, eds. (Academic Press, 2015), pp. 169–201.
5. A. Glasser, M. A. Croft, and P. L. Kaufman, "Aging of the Human Crystalline Lens and Presbyopia," *Int. Ophthalmol. Clin.* **41**(2), 1–15 (2001).
6. P. J. Donaldson, A. C. Grey, B. Maceo Heilman, J. C. Lim, and E. Vaghefi, "The physiological optics of the lens," *Prog. Retinal Eye Res.* **56**, e1–e24 (2017).
7. N. A. Brown, A. J. Bron, and J. M. Sparrow, "An estimate of the size and shape of the human lens fibre in vivo," *Br. J. Ophthalmol.* **71**(12), 916–922 (1987).
8. J. R. Kuszak, "The Ultrastructure of Epithelial and Fiber Cells in the Crystalline Lens," *Int. Rev. Cytol.* **163**, 305–350 (1995).
9. V. L. Taylor, K. J. al-Ghoul, C. W. Lane, V. A. Davis, J. R. Kuszak, and M. J. Costello, "Morphology of the normal human lens," *Invest. Ophthalmol. Vis. Sci.* **37**(7), 1396–1410 (1996).

10. J. R. Kuszak, R. K. Zoltoski, and C. E. Tiedemann, "Development of lens sutures," *Int. J. Dev. Biol.* **48**(8-9), 889–902 (2004).
11. J. R. Kuszak, B. A. Bertram, and J. L. Rae, "The Ordered Structure of the Crystalline Len," in *Development of Order in the Visual System. Cell and Developmental Biology of the Eye*, S. R. Hilfer and J. B. Sheffield, eds. (Springer, 1986), pp. 35–60.
12. U. P. Andley, "Crystallins in the eye: Function and pathology," *Prog. Retinal Eye Res.* **26**(1), 78–98 (2007).
13. D. C. Beebe, "Maintaining transparency: a review of the developmental physiology and pathophysiology of two avascular tissues," *Semin. Cell Dev. Biol.* **19**(2), 125–133 (2008).
14. H.-T. D. Wu, L. A. Howse, and E. Vaghefi, "Effect of Age-Related Human Lens Sutures Growth on Its Fluid Dynamics," *Invest. Ophthalmol. Visual Sci.* **58**(14), 6351–6357 (2017).
15. G. Duncan, I. M. Wormstone, and P. D. Davies, "The aging human lens: structure, growth, and physiological behaviour," *Br. J. Ophthalmol.* **81**(10), 818–823 (1997).
16. A. J. Bron, G. F. J. M. Vrensen, J. Koretz, G. Maraini, and J. J. Harding, "The Ageing Lens," *Ophthalmologica* **214**(1), 86–104 (2000).
17. R. Michael and A. J. Bron, "The ageing lens and cataract: a model of normal and pathological ageing," *Philos. Trans. R. Soc., B* **366**(1568), 1278–1292 (2011).
18. N. Pescosolido, A. Barbato, R. Giannotti, C. Komaiha, and F. Lenarduzzi, "Age-related changes in the kinetics of human lenses: prevention of the cataract," *Int. J. Ophthalmol. (Engl. Ed.)* **9**(10), 1506–1517 (2016).
19. C. Cheng, J. Parreno, R. B. Nowak, S. K. Biswas, K. Wang, M. Hoshino, K. Uesugi, N. Yagi, J. A. Moncaster, W.-K. Lo, B. Pierscionek, and V. M. Fowler, "Age-related changes in eye lens biomechanics, morphology, refractive index and transparency," *Aging* **11**(24), 12497–12531 (2019).
20. J. R. Kuszak, J. G. Sivak, and J. A. Weerheim, "Lens optical quality is a direct function of lens sutural architecture," *Invest. Ophthalmol. Vis. Sci.* **32**(7), 2119–2129 (1991).
21. R. Navarro and M. Angeles Losada, "Shape of stars and optical quality of the human eye," *J. Opt. Soc. Am. A* **14**(2), 353–359 (1997).
22. M. Dubbelman, G. L. Van der Heijde, H. A. Weeber, and G. F. J. M. Vrensen, "Changes in the internal structure of the human crystalline lens with age and accommodation," *Vision Res.* **43**(22), 2363–2375 (2003).
23. J. G. Sivak, K. L. Herbert, K. L. Peterson, and J. R. Kuszak, "The Interrelationship of Lens Anatomy and Optical Quality I. Non-primate Lenses," *Exp. Eye Res.* **59**(5), 505–520 (1994).
24. J. R. Kuszak, K. L. Peterson, J. G. Sivak, and K. L. Herbert, "The Interrelationship of Lens Anatomy and Optical Quality II. Primate Lenses," *Exp. Eye Res.* **59**(5), 521–535 (1994).
25. A. Gargallo, J. Arines, and E. Acosta, "Lens aberrations and their relationship with lens sutures for species with Y-suture branches," *J. Biomed. Opt.* **18**(2), 025003 (2013).
26. J. F. Koretz, C. A. Cook, and J. R. Kuszak, "The zones of discontinuity in the human lens: Development and distribution with age," *Vision Res.* **34**(22), 2955–2962 (1994).
27. J. R. Kuszak and K. J. Al-Ghoul, "A Quantitative Analysis of Sutural Contributions to Variability in Back Vertex Distance and Transmittance in Rabbit Lenses as a Function of Development, Growth, and Age," *Optom. Vis. Sci.* **79**(3), 193–204 (2002).
28. J. R. Kuszak, J. G. Sivak, K. L. Herbert, S. Scheib, W. Garner, and G. Graff, "The Relationship Between Rabbit Lens Optical Quality and Sutural Anatomy after Vitrectomy," *Exp. Eye Res.* **71**(3), 267–281 (2000).
29. K. J. Al-Ghoul, R. K. Nordgren, A. J. Kuszak, C. D. Freel, M. J. Costello, and J. R. Kuszak, "Structural Evidence of Human Nuclear Fiber Compaction as a Function of Ageing and Cataractogenesis," *Exp. Eye Res.* **72**(3), 199–214 (2001).
30. J. R. Kuszak, B. A. Bertram, M. S. Macsai, and J. L. Rae, "Sutures of the Crystalline Lens: A Review," *Scan. Electron Microsc.* **III**, 1369–1378 (1984).
31. B. R. Masters, "Confocal microscopy of the in-situ crystalline lens," *J. Microsc.* **165**(1), 159–167 (1992).
32. J. R. Kuszak, M. Mazurkiewicz, L. Jison, A. Madurski, A. Ngando, and R. K. Zoltoski, "Quantitative analysis of animal model lens anatomy: accommodative range is related to fiber structure and organization," *Vet. Ophthalmol.* **9**(5), 266–280 (2006).
33. R. B. Nowak, R. S. Fischer, R. K. Zoltoski, J. R. Kuszak, and V. M. Fowler, "Tropomodulin1 is required for membrane skeleton organization and hexagonal geometry of fiber cells in the mouse lens," *J. Cell Biol.* **186**(6), 915–928 (2009).
34. E. Acosta, J. Bueno, C. Schwarz, and P. Artal, "Relationship between wave aberrations and histological features in ex vivo porcine crystalline lenses," *J. Biomed. Opt.* **15**(5), 055001 (2010).
35. Y. Shi, A. De Maria, T. Bennett, A. Shiels, and S. Bassnett, "A Role for EphA2 in Cell Migration and Refractive Organization of the Ocular Lens," *Invest. Ophthalmol. Visual Sci.* **53**(2), 551–559 (2012).
36. J. Parreno, C. Cheng, R. B. Nowak, and V. M. Fowler, "The effects of mechanical strain on mouse eye lens capsule and cellular microstructure," *Mol. Biol. Cell* **29**(16), 1963–1974 (2018).
37. A. Roorda and A. Glasser, "Wave aberrations of the isolated crystalline lens," *J. Vis.* **4**(4), 1 (2004).
38. J. Sukhija and S. Kaur, "Congenital Sutural Cataract," *N. Engl. J. Med.* **371**(18), e27 (2014).
39. J. Jinagal, G. Gupta, and F. Thattaruthody, "Sutural cataract," *Indian J. Ophthalmol.* **66**(6), 853 (2018).
40. J. J. Liu, I. Grulkowski, M. F. Kraus, B. Potsaid, C. D. Lu, B. Baumann, J. S. Duker, J. Hornegger, and J. G. Fujimoto, "In vivo imaging of the rodent eye with swept source/Fourier domain OCT," *Biomed. Opt. Express* **4**(2), 351–363 (2013).

41. A. de Castro, A. Benito, S. Manzanera, J. Mompeán, B. Cañizares, D. Martínez, J. M. Marín, I. Grulkowski, and P. Artal, "Three-Dimensional Cataract Crystalline Lens Imaging With Swept-Source Optical Coherence Tomography," *Invest. Ophthalmol. Visual Sci.* **59**(2), 897–903 (2018).
42. I. Grulkowski, S. Manzanera, L. Cwiklinski, J. Mompeán, A. de Castro, J. M. Marín, and P. Artal, "Volumetric macro- and micro-scale assessment of crystalline lens opacities in cataract patients using long-depth-range swept source optical coherence tomography," *Biomed. Opt. Express* **9**(8), 3821–3833 (2018).
43. K. Zuiderveld, "Contrast limited adaptive histogram equalization," in *Graphics Gems IV*, P. S. Heckbert, ed. (Academic Press, San Diego, 1994), pp. 474–485.
44. M. H. F. Wilkinson, "Automated and manual segmentation techniques in image analysis of microbes," in *Digital Image Analysis of Microbes: Imaging Morphometry, Fluorometry and Motility Techniques and Applications*, F. Schut and M. H. F. Wilkinson, eds. (Wiley, 1998), pp. 135–171.
45. C. Y. Suen and T. Y. Zhang, "A Fast Parallel Algorithm for Thinning Digital Patterns," *Commun. ACM* **27**(3), 236–239 (1984).
46. A. L. Wong, C. K.-S. Leung, R. N. Weinreb, A. K. C. Cheng, C. Y. L. Cheung, P. T.-H. Lam, C. P. Pang, and D. S. C. Lam, "Quantitative assessment of lens opacities with anterior segment optical coherence tomography," *Br. J. Ophthalmol.* **93**(1), 61–65 (2009).
47. A. de Castro, S. Ortiz, E. Gamba, D. Siedlecki, and S. Marcos, "Three-dimensional reconstruction of the crystalline lens gradient index distribution from OCT imaging," *Opt. Express* **18**(21), 21905–21917 (2010).
48. I. Grulkowski, J. J. Liu, B. Potsaid, V. Jayaraman, C. D. Lu, J. Jiang, A. E. Cable, J. S. Duker, and J. G. Fujimoto, "Retinal, anterior segment and full eye imaging using ultrahigh speed swept source OCT with vertical-cavity surface emitting lasers," *Biomed. Opt. Express* **3**(11), 2733–2751 (2012).
49. M. Sun, J. Birkenfeld, A. de Castro, S. Ortiz, and S. Marcos, "OCT 3-D surface topography of isolated human crystalline lenses," *Biomed. Opt. Express* **5**(10), 3547–3561 (2014).
50. P. Pérez-Merino, M. Velasco-Ocana, E. Martínez-Enriquez, and S. Marcos, "OCT-based crystalline lens topography in accommodating eyes," *Biomed. Opt. Express* **6**(12), 5039–5054 (2015).
51. I. Grulkowski, S. Manzanera, L. Cwiklinski, F. Sobczuk, K. Karnowski, and P. Artal, "Swept source optical coherence tomography and tunable lens technology for comprehensive imaging and biometry of the whole eye," *Optica* **5**(1), 52–59 (2018).
52. D. G. Cogan, "Anatomy of Lens and Pathology of Cataracts," *Exp. Eye Res.* **1**(4), 291–IN3 (1962).
53. J. R. Kuszak, R. K. Zoltoski, and C. Sivertson, "Fibre cell organization in crystalline lenses," *Exp. Eye Res.* **78**(3), 673–687 (2004).
54. E. Vaghefi, B. P. Pontre, M. D. Jacobs, and P. J. Donaldson, "Visualizing ocular lens fluid dynamics using MRI: manipulation of steady state water content and water fluxes," *Am. J. Physiol. Regul. Integr. Comp. Physiol.* **301**(2), R335–R342 (2011).
55. E. Vaghefi, K. Walker, B. P. Pontre, M. D. Jacobs, and P. J. Donaldson, "Magnetic resonance and confocal imaging of solute penetration into the lens reveals a zone of restricted extracellular space diffusion," *Am. J. Physiol. Regul. Integr. Comp. Physiol.* **302**(11), R1250–R1259 (2012).
56. M. Guillon, K. Dumbleton, P. Theodoratos, M. Gobbe, C. B. Wooley, and K. Moody, "The Effects of Age, Refractive Status, and Luminance on Pupil Size," *Optom. Vis. Sci.* **93**(9), 1093–1100 (2016).